Nuclear Instruments and Methods in Physics Research A 664 (2012) 193–202

Contents lists available at SciVerse ScienceDirect

Nuclear Instruments and Methods in Physics Research A

journal homepage: www.elsevier.com/locate/nima

Performance of a proton irradiation chamber

S. Agosteo [a,b], E. Borsato [c,d], F. Dal Corso [c], A. Fazzi [a,b], F. Gonella [c], M.V. Introini [a,b], I. Lippi [c,1], M. Lorenzoli [a,b], L. Modenese [c], F. Montecassiano [c], M. Pegoraro [c], A. Pola [a,b], V. Varoli [a,b], P. Zotto [c,d,*]

[a] INFN, Sezione di Milano, via Celoria 16, 20133 Milano, Italy
[b] Politecnico di Milano, Dipartimento di Energia, Sezione di Ingegneria Nucleare—CeSNEF, via Ponzio 34/3 20133 Milano, Italy
[c] INFN, Sezione di Padova, via Marzolo 8, 35131 Padova, Italy
[d] Università di Padova, Dipartimento di Fisica, via Marzolo 8, 35131 Padova, Italy

ARTICLE INFO

Article history:
Received 12 July 2011
Received in revised form
29 September 2011
Accepted 14 October 2011
Available online 9 November 2011

Keywords:
Radiation tests
Electronics radiation resistance
Total dose resistance

ABSTRACT

A Proton Irradiation Chamber aiming to perform radiation tests of electronic components was developed. The precision on the measurement of the ion currents was pushed beyond the resolution of the picoammeter by means of a series of collimators on the beam showing a linear correlation among the currents measured on them and the smaller, not measurable, current on the target. As an example of the obtained results the tests done on a Si microdosimeter and a power p-MOS are reported.

1. Introduction

The Proton Irradiation Chamber is a Faraday cup that was developed to cope with some use cases at the 7 MV Van de Graaf accelerator at INFN National Laboratories, Legnaro (PD), Italy:

- measurements with neutrons obtained by proton scattering on a target (thick Be, LiF),
- direct irradiation of semiconductor detectors,
- radiation resistance tests.

The achievement of a trustable measurement of the ion current hitting the target is important in any of these tests. It must be directly measured in the first case and indirectly obtained in the other two. In the direct irradiation tests the estimate must be in the picoampere range or even below.

The chamber, shown in Fig. 1, is built using several blocks in order to fulfill the requirements.

The first block is a set of three collimators system (C1, C2 and C3) made of a 0.25 mm thick tantalum foil with circular holes of 5 mm, 2.5 mm and 0.5 mm diameter respectively. In the standard setup collimator C3 is in fact composed by two identical collimators put at 4 cm distance, whose main task is the reduction of the beam divergence, but it is useful also to reduce beam intensity. It can be replaced by a single tantalum collimator with an hole diameter dependent on the required size of the irradiation area. The collimator block is followed by a removable beam stopper (C4) made of a 0.25 cm tantalum foil intercepting the collimated beam and is used for tests and calibration. Each collimator and the beam stopper are readout independently. C4 can be replaced by any required target in order to allow measurements for the first foreseen use case. The last block is put on a movable arm and is made of two pieces: the detector to be tested and an alignment system (Q) composed by four tantalum quadrants, each one readout independently, delimiting a cross shaped region. The cross center is put at known distance from the detector measured with a laser beam. Both movable arms are remotely controlled by a step motor. The minimum step is 5.2 mrad ($\simeq 0.3^\circ$) equivalent to $\simeq 0.5$ mm displacement of the detector block and the movements spans the full $\pm 90^\circ$ range with respect to the beam axis.

The beam size is limited by a 10 mm diameter tantalum collimator put on the beam line before the irradiation chamber.

The set-up procedure is the following.

When beam is set on, the beam stopper and the alignment cross are put on the beam trajectory. Then C4 is removed, once verified that the beam really hits it, so that the beam hits the alignment cross. The beam is aligned when the current readings of each tantalum quadrant is about equal, that is when moving the cross by one step the beam is mainly within one of the tantalum elements instead of being shared among all four elements. This operation is fast and easy using a well focused

* Corresponding author at: INFN, Sezione di Padova, via Marzolo 8, 35131 Padova, Italy. Tel.: +39 0498277052; fax: +39 0498277201.
E-mail address: pierluigi.zotto@pd.infn.it (P. Zotto).
[1] Now on leave.

0168-9002/$ - see front matter © 2011 Elsevier B.V. All rights reserved.
doi:10.1016/j.nima.2011.10.062

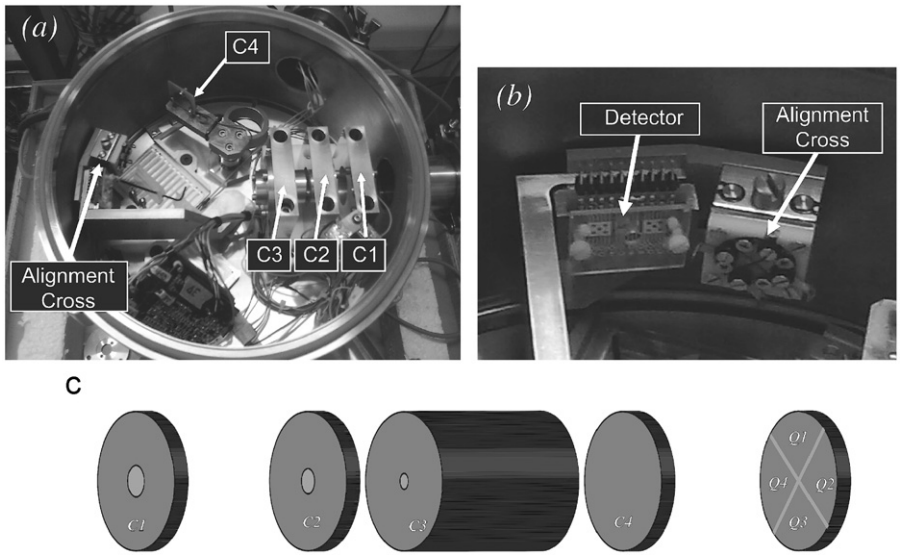

Fig. 1. Pictures of the Proton Irradiation Chamber: (a) overview of the chamber; (b) detail of the detector arrangement; (c) sketch of the set-up.

beam with a current around 300–400 pA on C4. The detector is then moved to the measurement position applying its known displacement with respect to Q. The precision of the positioning system is around 0.5 mm.

2. Description of the picoammeter

The picoammeter is a system refurbished from the radiation monitoring apparatus of the ZEUS [1,2] experiment. It consists essentially of a VME board housing eight current input ADC channels with a nominal resolution of 0.7 pA and a full scale of about 700 nA. It is designed around the BurrBrown device DDC112, which is a charge integrating 20 bit ADC widely programmable in full scale charge and integration time; we used it at the maximum range (350 pC) with minimum integration time (500 μs). The device can act as a continuous integrator, without dead time, since it has two integrators working in interlaced mode; while one is integrating, the other is being digitized.

Each DDC112 chip houses two channels, so the board is equipped with four devices. Having serial readout, the digitized data must be parallelized and then stored into a FIFO. In order to maintain the continuity of the current integration, the readout of the channels must be opportunely interlaced and synchronized with the FIFO writing. The management of the very complex control signals of the ADCs and FIFOs is implemented into a FPGA. Every 500 μs eight (one per channel) 20 bits long words are written into the FIFO; the data are packaged in 'data frames' containing 32 words (four readings per channel). When a data frame is ready (every 2 ms) the board sends an interrupt request to the CPU. The FIFO can contain up to seven data frames; the CPU must take care of servicing the interrupt requests without allowing FIFO overflows (in that extreme case a reset must be issued).

Due to the very high sensitivity of the device, big care must be devoted to the design of the channels input layout; moreover the board should be operated at stabilized temperature and should be recalibrated from time to time, to overcome the temperature and time drift of the ADC parameters. The calibration of the picoammeter is done comparing its readout against measurements performed by a Keithley 6487 picoammeter/voltage source.

Fig. 2 shows, as an example, the calibration data of one channel: the integral linearity of the device is really excellent over its whole range. The ADC characteristic is obtained reversing

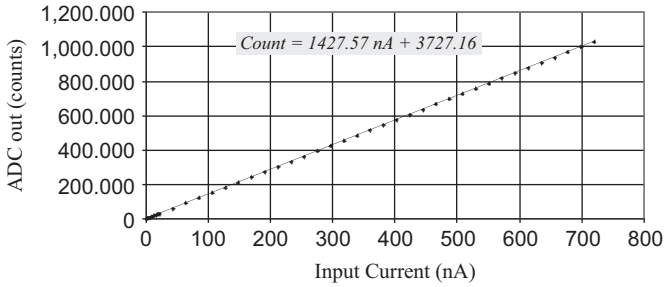

Fig. 2. Calibration of a DDC112 channel versus the current measured by a Keithley 6487.

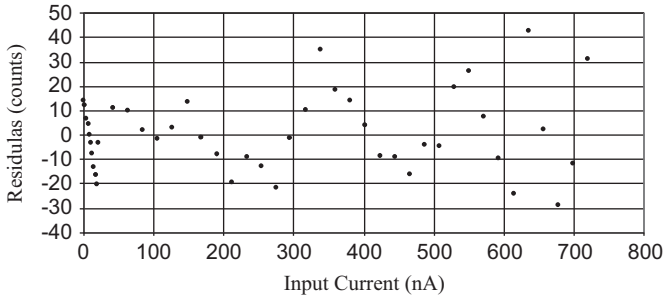

Fig. 3. Residuals of the line fit to calibration plot.

the fit equation shown in Fig. 2

$$I = 7.005^{pA/_{count}} - 2.611 \text{ nA}. \quad (1)$$

The same quality cannot be asserted about the differential linearity, as shown by Fig. 3, but the clear non-random deviations (particularly evident close to the origin) are mostly due to the Keithley 6487 itself, as can be easily verified by looking at the current measurements performed through a calibrated resistor.

The noise affecting the measurements was estimated by the standard deviation of the single measurement (that is, as stated, an integration over 500 μs) which varies in the range 10–13 pA from channel to channel. All the measurements performed in our tests are software averaged over 1 s, i.e. over 2000 hardware measurements, so the resolution of our acquired data is better than 0.3 pA.

This resolution is referred to the instrument connected to the chamber through 5 m long coax cables, in the experimental area.

3. Estimation of the beam intensity on detector

The estimation of the particle fluence on the detector is relevant for direct irradiations and non-metallic targets, since the current on any metallic target can be directly measured. In the ideal case of a flat beam profile it is a simple geometric exercise, while it needs a calibration otherwise. The flattest profile is obtained by beam defocusing which at the used accelerator implies losing up to 70% of the produced ions. Even in this situation the beam is quite unstable and with the same parameters the beam controls miss repeatability on a daily basis (the accelerator does not work continuously: it is switched on in the morning and off in the evening of every working day). Furthermore the relative alignment between the two collimators in C3 was unpredictable, since the Irradiation Chamber was installed and removed after each test. Hence a daily calibration is required for a trustable estimation of the ions fluence on the detector.

The easiest estimation method implies finding a functional relationship between the current on C4 and the current in any of the collimators. Fitting this relationship on calibration data and using it once C4 is removed would solve the problem. Practically, since an extrapolation must be done, the method is usable only if the law is linear. Fig. 4 shows that this is indeed the case: the average current measured in short runs at different beam intensities by any of the collimators and the beam stopper roughly follows a proportional law, showing also that the current on C4 becomes rapidly unmeasurable. The linear nature of the relationship allows a safe extrapolation to lower currents once it is determined at higher currents. The extrapolation can be trusted until the current on C3 is measurable. The error is minimized by averaging the estimate given by the three available relations

$$i_4 = \frac{f_1(i_1)+f_2(i_2)+f_3(i_3)}{3} \quad (2)$$

and the systematic error can be assumed as the range delimited by single estimates. The sharing of the beam current among the collimators and C4 is reported in Table 1. The sharing factors are rather stable and the average value is closer to the geometrical expectation for the three collimators, while for C4 it is substantially different. Most of the difference is justified by the peculiar shape of C3: the beam direction and the line defined by the two holes in C3 must be perfectly aligned in order to meet the geometrical factor and this is rather difficult to achieve. A closer look to the data shows

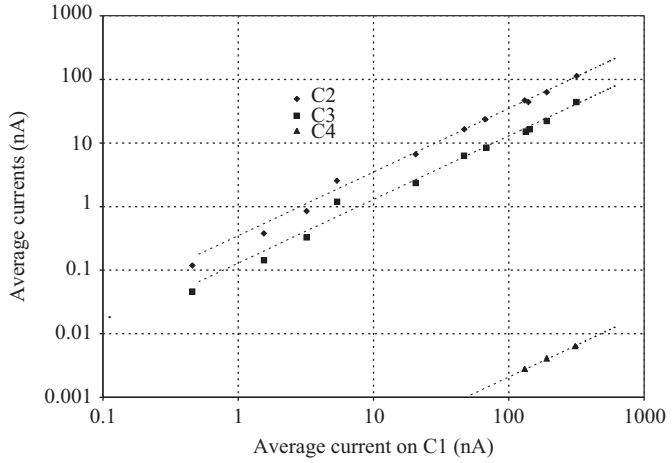

Fig. 4. Correlation between the average current measured in C1 and the average current measured in C2, C3 and C4.

Table 1
Sharing of the beam current among collimators and beam stopper. The sharing factors are compared to the geometrically expected fractions.

i_1 (nA)	i_2 (nA)	i_3 (nA)	i_4 (nA)	i_T (nA)	i_1/i_T (%)	i_2/i_T (%)	i_3/i_T (%)	i_4/i_T (%)
146.250	39.760	12.740	0.018	198.768	73.58	20.00	6.41	0.0092
125.280	34.500	11.060	0.016	170.856	73.32	20.19	6.47	0.0094
93.420	26.020	8.380	0.012	127.832	73.08	20.35	6.56	0.0094
78.820	22.350	7.340	0.011	108.521	72.63	20.60	6.76	0.0101
Average factors					73.15	20.29	6.55	0.0095
Geometrical factors					73.43	19.93	6.38	0.2700

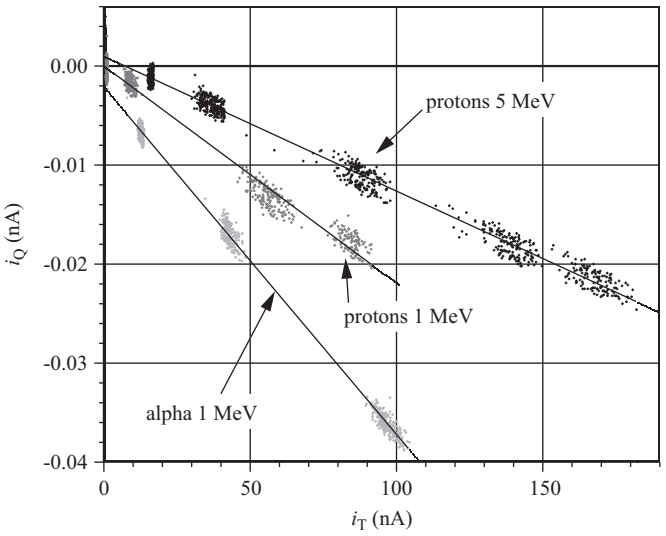

Fig. 5. Current measured in the alignment cross quadrants as a function of incident beam current for different ions and energies.

other interesting details. The quadrants delimiting the alignment cross are always read out and should show a null current when Q is screened by the beam stopper. It is instead behaving as shown in Fig. 5, where a non-negligible negative current dependent on the incident beam intensity is observed. The current intensity depends also on the type of incident particle and on its energy.

The only found explanation is the production of δ-rays extracted from the tantalum targets by the incident ion. These electrons are then randomized since they can scatter around traveling long distances due to the vacuum inside the chamber ($\simeq 10^{-8}$ torr). Another contribution can come from electrons produced by X-ray or γ-ray interactions with the material inside the chamber.

These electrons indeed behave like a gas filling uniformly the Proton Irradiation Chamber as shown in Fig. 6, where the measurement was repeated with the alignment cross in different positions with respect to the beam line. The vertical lines on the plot delimit measurements taken in each position. The ratio of the current on Q to the total current on the collimators (left axis) is about constant, independent of the measurement cross position, so that it is sensible to conclude that there is no dependence on its position, supporting the hypothesis of the presence of an electron gas. The right axis shows the total current measured on the collimators block showing its sudden variations although the beam parameters were not changed. The ratio is anyway stable suggesting that the correlation between the current on the cross and the total current remains anyway unchanged.

The flux of electrons on the alignment cross is in the picoampere range and, since the area of the beam stopper is comparable to the area of the quadrants, it modifies by a non-negligible amount the actual current of the beam stopper. The current on

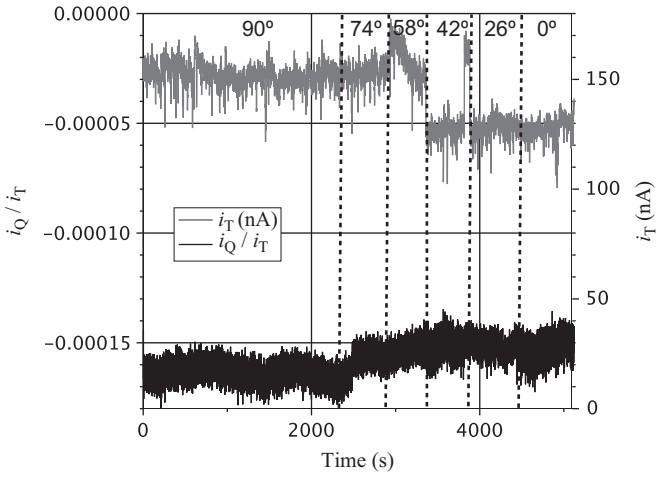

Fig. 6. Sum of the ratio between current on the four quadrants of the alignment cross and current on C1 in a position scan. See text for a careful interpretation.

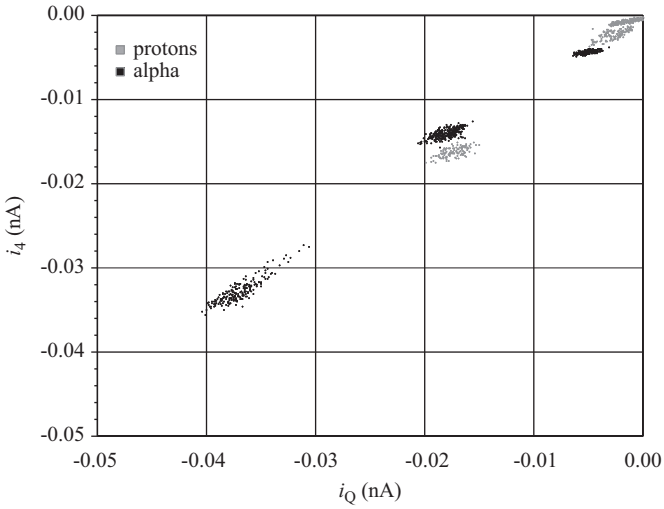

Fig. 7. The current on C4 versus the current on the alignment cross when they are both screened by beam.

Q and C4, when they are both away from the beam line is shown in Fig. 7. There is a direct proportionality between the two measurements due to the difference in effective cross-section. The proportional factor is $f_Q \simeq 0.864$ substantially independent of the incident particle nature and energy.

Unfortunately the instability and the non-repeatability linked to the daily performance of the accelerator reflects also on the current measured on Q that shows a dependency on the day (Fig. 8) that hence must enter in the calibration procedure.

The calibration must give a reliable prediction below the actual measurements possible in C4 and proceeds as follows. The beam current is varied in the trustable C4 measurement range (>1 pA), reading out all the eight available channels (C1, C2, C3, C4, Q1, Q2, Q3, Q4). The current on C4 is assumed to be the combination of the one actually measured in C4 and the one measured in Q (sum of Q1, Q2, Q3 and Q4 corrected by the previously introduced effective cross-section factor f_Q)

$$i_{4,rec} = i_4 - f_Q \sum_{k=1}^{4} Q_k. \tag{3}$$

The correlation between the current reconstructed on C4 and the current on C3 as measured in different days is reported in Fig. 9. The

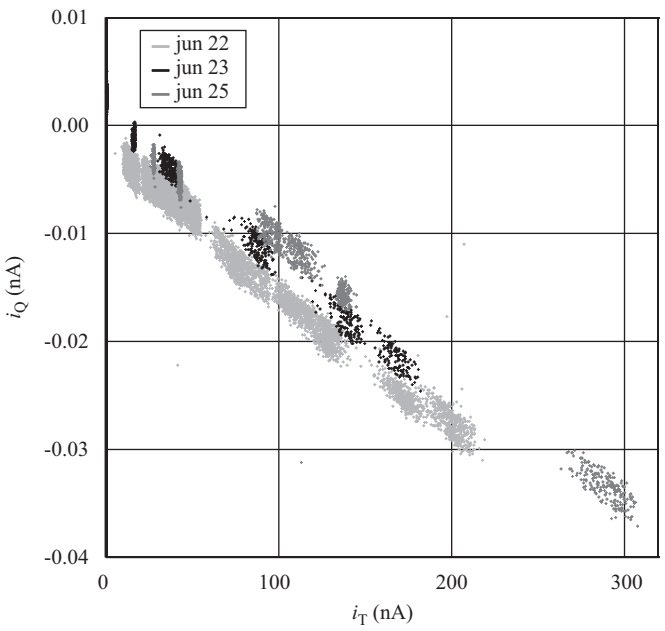

Fig. 8. Daily dependence of the Q current on the beam current.

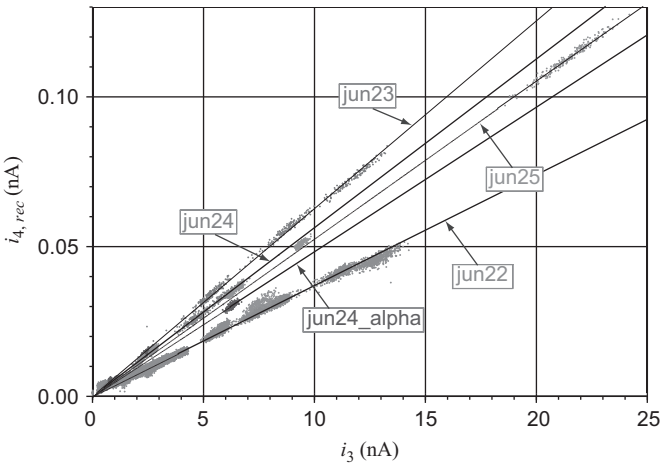

Fig. 9. Correlation between the current on C4 as reconstructed by the calibration algorithm and the current measured in C3. The different colors and fitted lines refer to different days of data taking.

seen daily variation is associated to the already reported unpredictability of the status of the machine every time it is brought back to operation. Apart from this problem, which forces a daily calibration, there is always a simple proportional law to be determined.

The same situation occurs correlating the reconstructed current on C4 with the current measured in C1 and C2 as shown in Fig. 10. Since the assumption of a flat beam does not hold exactly, the proportional relation is less tight with increasing effective area, but assuming its validity is anyway a good approximation.

Hence three coefficients are determined from these plots and the estimate of the current on the detector is given by the average of the three determinations.

The statistical precision of the estimation is around 2 pA as shown by the residuals to the proportional fit (Fig. 11). The small value of the statistical error indicates that the fluence measurement on long runs is dominated by systematic effects like beam instability. A good index of the systematic error is the difference among the average value and the values given by each collimator independently. This difference can be safely assumed as the

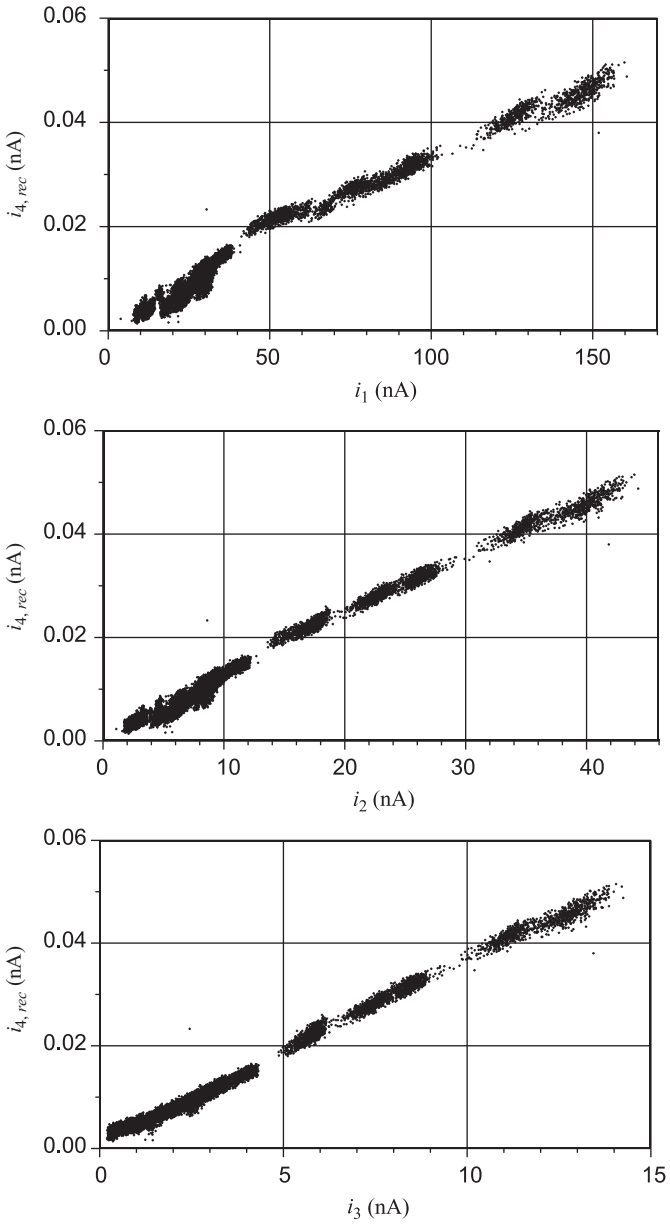

Fig. 10. Correlation between the current reconstructed in C4 and the current measured on any collimator.

systematic error. Its value is not stable but it is normally in the 2–10% range depending on beam performance.

In order to estimate the fluence it is compulsory to determine the size of the beam spot. This can be done measuring the rate of interactions on the detector as a function of its position with respect to the beam axis.

The signals were counted in coincidence on two coupled silicon sensors (the microdosimeter described in Section 4). The step of the position scan was 5.2 mrad corresponding to about 0.5 mm displacement of the detector.

The relative rates measured at fixed thresholds for two different nominal currents are shown in Fig. 12.

The interpolated function is the simple symmetric parameterization

$$F(\theta) = \frac{A}{e^{-B(\theta-C)} + e^{B(\theta-C)}} + D. \quad (4)$$

The size of the irradiated region (diameter of the beam spot) measured as the FWHM of the distributions is about 20 mrad ($\simeq 2$ mm) in complete agreement with the geometrical expectations, when considering beam divergence, thus covering the full detector. The small size of the effective beam spot allows only measurements for very small devices as opposed to the main facilities available in nuclear laboratories.[2]

4. Radiation tests

We made total dose effects radiation tests of few samples of different devices: a silicon device to be used as a microdosimeter [6] and IRF7425, a vertical HEXFET power p-MOS to be used in the CMS experiment [7] at LHC to upgrade the Muon Trigger [8].

4.1. Results of microdosimeter irradiation

The device cross-section is shown in Fig. 13. It is a silicon telescope composed by two sensitive stages: the first stage (named ΔE) is a very thin ($\simeq 1$ μm) p-type layer meant to measure proton dE/dx, while the second stage (named E) is a 500 μm thick n-type layer measuring the proton energy.

We irradiated four detectors set at fixed voltage ($V_E =$ 60 Ve$V_{\Delta E} = 5$ V) with 5 MeV protons. The leakage currents were continuously monitored during the irradiation which was interrupted from time to time in order to record the I–V characteristics of both stages. The current measured on the E stage includes also the current circulating on the guard rings, while the current measured on the ΔE stage is the actual one. Detector B and D were irradiated during a single session while detectors A and C were irradiated in two sessions after annealing at room temperature (1 month after $\simeq 6.19 \times 10^{11}$ p/cm^2 fluence for detector A and 2 days after $\simeq 9.48 \times 10^{11}$ p/cm^2 fluence for detector C). The typical irradiation time between two I–V measurements (lasting $\simeq 5$–10 min each) was 10–15 min. The temperature inside the Proton Irradiation Chamber is rather stable in the range 22–24 °C.

The fluence on the stages is obviously the same for each irradiation (the final one was $\simeq 2 \times 10^{12}$ p/cm^2 for each detector), but this is not the case for the absorbed dose, because while the proton passes through the ΔE stage leaving a low amount of energy, it is completely absorbed in the E stage.

The detector is biased through a filter circuit where the current is limited by a 110 MΩ resistor in series with the detector. Hence a large leakage current implies a non-negligible voltage drop on the resistor causing a non-negligible difference between the actual detector bias and the voltage applied by the power supply. The filter capacitor is guaranteed only up to 200 V, therefore the power supply cannot be set beyond this limit.

We explored the full range of applied voltage only during detector D test. Then we give a full report only for detector D where we could in fact compare the performance at fixed bias.

The power supply voltage we had to apply in order to guarantee V_{bias}=60 V on the E stage for detector D at any measured leakage current is shown in Fig. 14. Roughly the overvoltage needs to be changed at a rate $\simeq 2.5$ V/kGy. The overvoltage needed for the ΔE stage is only 0.2 V at the end of the irradiation. Hence the voltage correction during the detector operation is relevant only for the E stage, while it can be ignored for the ΔE stage.

[2] There are several irradiation facilities each one having different characteristics. We mention the ones we have used: PIF at PSI [3], SIRAD at LNL [4] and CYCLONE at UCL [5]. A list of facilities commonly used for tests of semiconductor devices for LHC can be found at http://rd50.web.cern.ch/rd50/irradiation/irradiation.html.

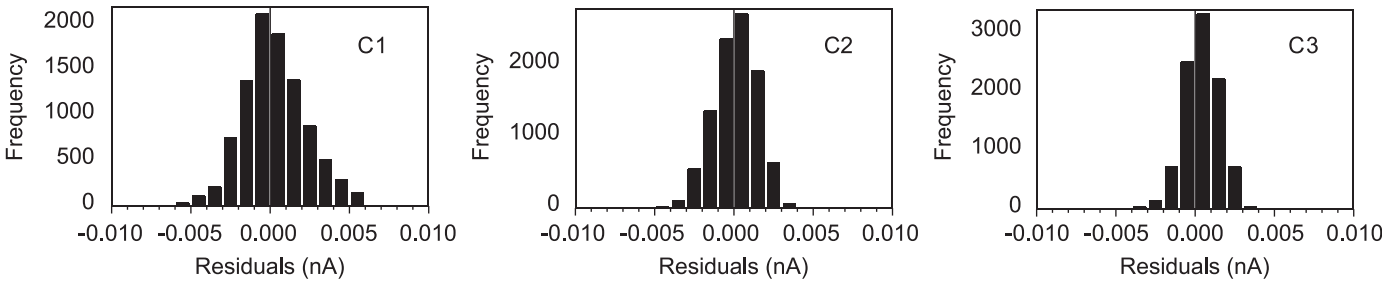

Fig. 11. Residuals to the calibration fit for each collimator.

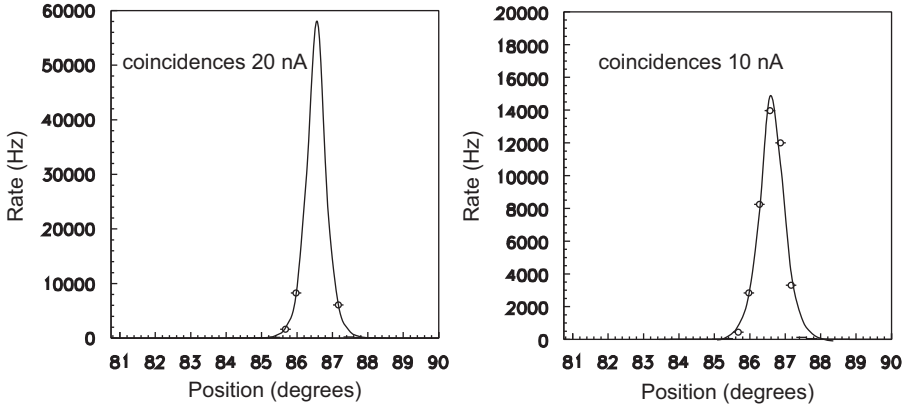

Fig. 12. Rate of the incident protons for coincidences of two coupled silicon sensors alone as a function of the position of the detector with respect to the beam axis at different nominal beam current.

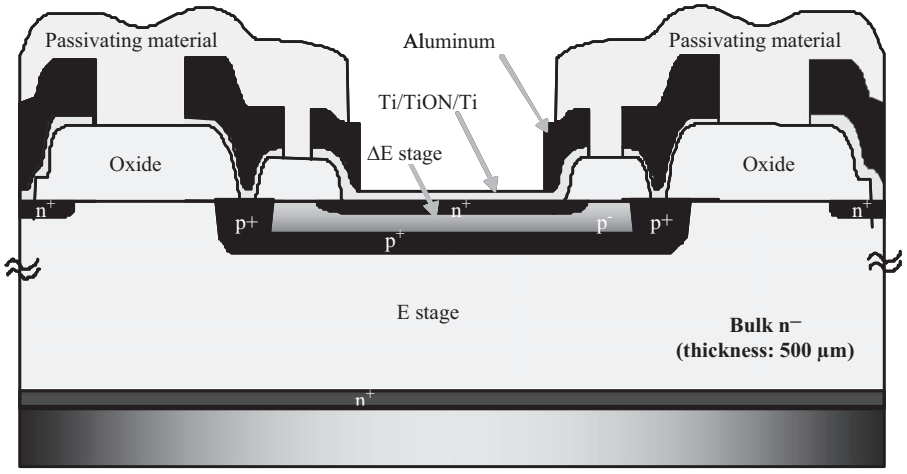

Fig. 13. Cross-section of the silicon telescope.

The *I–V* characteristics for detector D are shown in Fig. 15 for the *E* stage and Fig. 16 for the Δ*E* stage after correction for the voltage drop on the limiting resistor.

The leakage current at the nominal bias as function of the absorbed dose is reported in Fig. 17a and b for the two stages. Its absolute value change is quite different for the two stages, but its variation per unit volume, shown in Fig. 17c, should be comparable for the two stages and should be proportional to the fluence [9]. The dependence of the current density on fluence for the *E* stage is instead clearly flattening. We believe that this behavior is due to the influence of short time beneficial self-annealing [10] which is quite important while the *I–V* characteristic is being determined, due to the relatively long time required for the measurement. The same behavior is indeed reported in Ref. [11] if self-annealing corrections are not applied to the data. Another possible contribution to saturation can be related to damage surface currents, that we cannot separate from damage bulk currents, that are known to saturate after $\simeq 10$ kGy [12]. The damage rate constants are the slopes of the lines in Fig. 16c. Due to lack of information, it is impossible to apply self-annealing corrections to our data, but we can, in order to provide a first order evaluation of the damage rate, exclude from the fit the points clearly deviating from a line: the values of the fitted damage rate constants are $\alpha = 1.6 \times 10^{-16}$ A/cm for the *E* stage and $\alpha = 4.7 \times 10^{-17}$ A/cm for the Δ*E* stage. These values are consistent with the ones found in the literature [13]. The Δ*E* value is more reliable, since there is also an uncertainty on the effective detector volume of the *E* stage due to our measurements setup that includes the guard rings.

The current drawn by the E stage for all the irradiated detectors is shown in Fig. 18 as a function of the absorbed dose. Detector A was irradiated in two periods leaving a month for annealing at room temperature to see the extent of performance recovery. It indeed partially recovers, but it eventually behaves as detectors B and D. Detector C behaved like detector A, even if it was left annealing only for 2 days. The magnitude of the recovery was 56% for both detectors independently of the annealing time. Detector D was measured after 1 day annealing showing the same magnitude of recovery. The evidence of a very fast recovery supports our claim for an important contribution of self-annealing in the plot of Fig. 17c.

4.2. Results of the p-MOS irradiation

The energy available at the accelerator is not sufficient to irradiate commercial devices protected by epoxy resin. Then we reduced the epoxy thickness milling two IRF7425 samples in their center, with different sizes of the hole, in order to leave $\simeq 100\ \mu m$ resin. We could not reduce it further because the chip wire bondings are at that depth. Thus the devices were only partially exposed to the proton beam. A first estimation of the irradiated area was done removing completely the epoxy and checking visually on a microscope the size of the holes with respect to the full device, while its thickness was measured to be $\simeq 100\ \mu m$

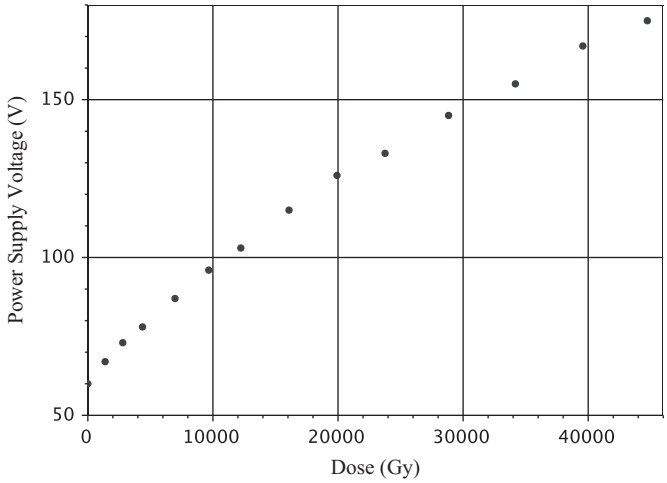

Fig. 14. Voltage to be applied to restore the same bias voltage before irradiation as a function of the absorbed dose for detector D.

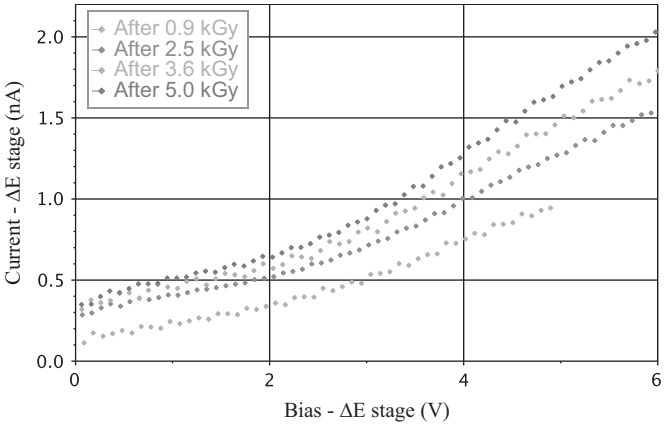

Fig. 16. I–V characteristics of the ΔE stage for detector D after different absorbed doses. The E stage is set at null voltage during the measurement.

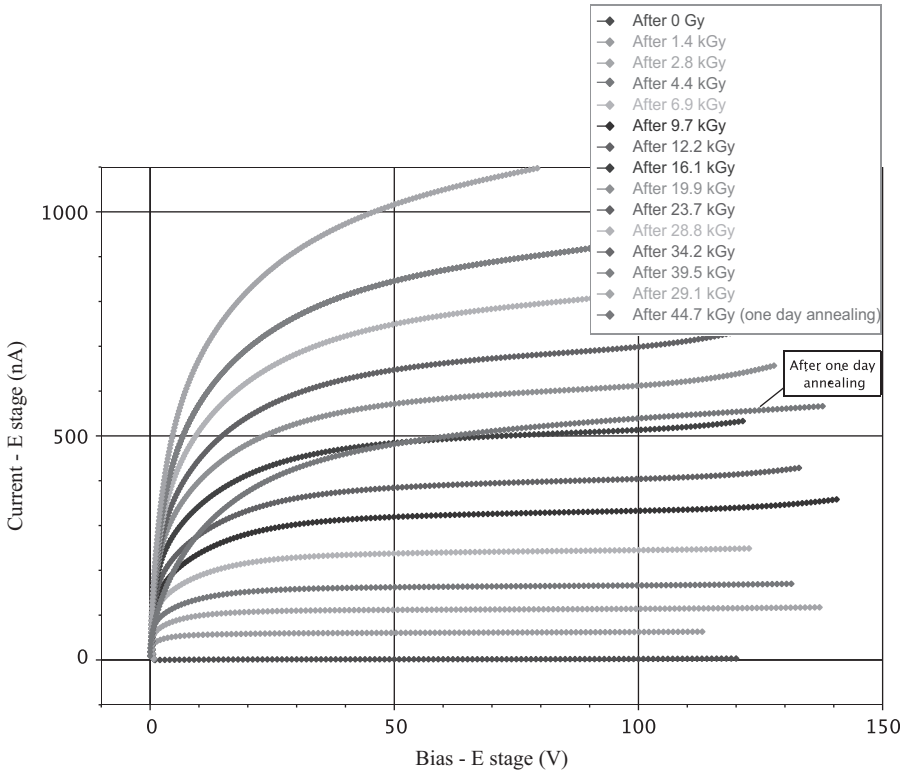

Fig. 15. I–V characteristics of the E stage for detector D after different absorbed doses. The ΔE stage is set at null voltage during the measurement. The measurement done before irradiation is barely visible close to the abscissa axis.

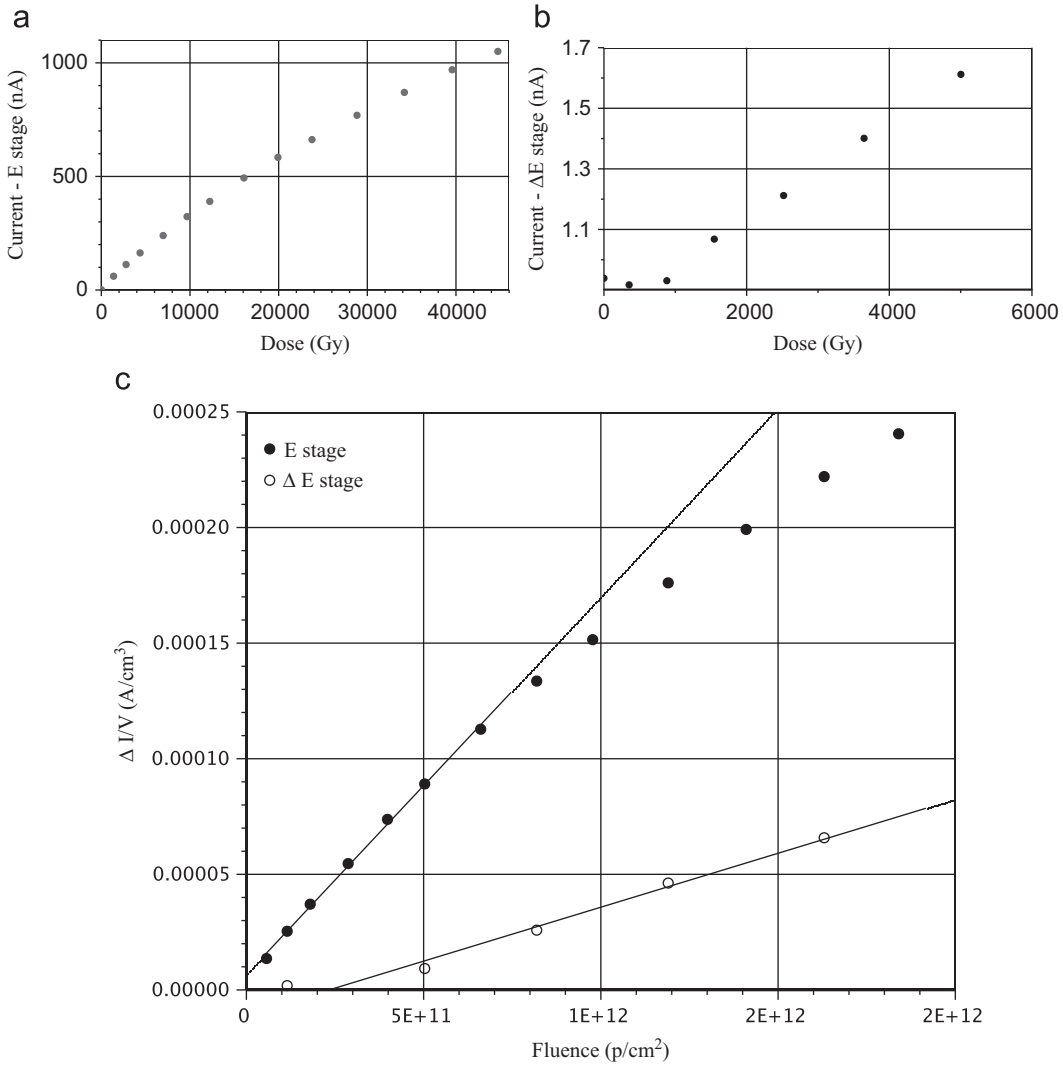

Fig. 17. Leakage current at $V_{bias} = 60$ V for detector D on the E stage (a) and at $V_{bias} = 4.8$ V on the ΔE stage (b) as a function of the absorbed dose. (c) Variation of the leakage current per unit volume as a function of the proton fluence for the two detector stages: the lines are a fit to evaluate the damage rate.

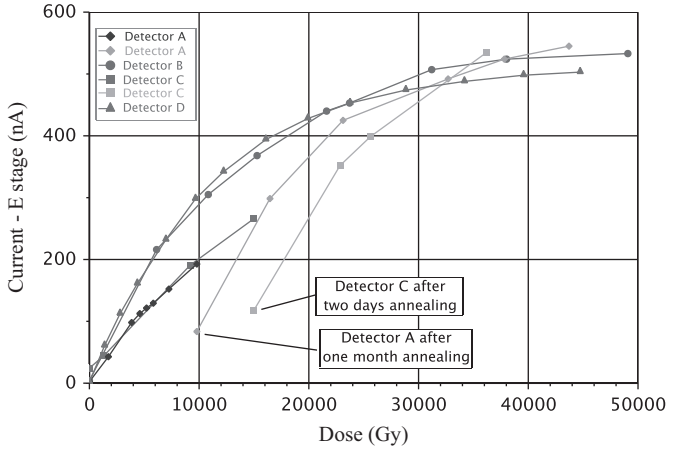

Fig. 18. Leakage current on the E stage at fixed power supply voltage (V = 60 V) after different radiation doses for two detectors.

after cutting the device. No further details about the p-MOS (e.g. process mode, number of elementary transistors, active silicon layers thickness) were available. We irradiated the two samples at energies of 5.5 MeV and 5 MeV respectively. The drain-source on-resistance (R_{on}) was constantly measured during irradiation. The recorded behavior of R_{on} during this partial irradiation of the device (R_{part}) as a function of the proton fluence F is plotted in Fig. 19. It was possible to extrapolate the measurement done with a partial irradiation in order to evaluate the damage on a fully irradiated device using the fact that the p-MOS is a device featuring a parallel transistors layout with a number of elementary MOSFETS that can be estimated $\geq 20,000/\text{mm}^2$ [14]. Indeed this topology, the measurement of resistance R_{on} before and during irradiation and the estimation on the fraction of irradiated area A can be used to allow the determination of the behavior of R_{on} with the fluence for a fully irradiated device.

Defining the quantities:

N	total number of elementary MOSFET connected in parallel
$R_{el}(F)$	resistance of one elementary MOSFET
A	fraction of irradiated area of the device
$R_0 = R_{el}(0)/N$	p-MOS on-source resistance before irradiation
$R_{full}(F) = R_{el}(F)/N$	p-MOS on-source resistance of a fully irradiated device

the measured resistance during a partial irradiation $R_{part}(F)$ can be expressed as the parallel equivalent of $k = N \cdot A$ irradiated elementary MOSFET with $j = N \cdot (1-A)$ ones not irradiated

$$R_{part}(F) = \frac{1}{\sum_1^k \frac{1}{R_{el}(F)} + \sum_1^j \frac{1}{R_{el}(0)}}. \quad (5)$$

Assuming that all irradiated MOSFETs behave in the same way we obtain

$$R_{part}(F) = \frac{1}{\frac{N \cdot A}{R_{el}(F)} + \frac{N \cdot (1-A)}{R_{el}(0)}} = \frac{1}{\frac{A}{R_{full}(F)} + \frac{1-A}{R_0}} = \frac{R_0 \cdot R_{full}(F)}{A \cdot R_0 + (1-A) R_{full}(F)}. \quad (6)$$

Inverting Eq. (6) we get the relationship

$$R_{full}(F) = \frac{A \cdot R_{part}(F)}{1-(1-A)\frac{R_{part}(F)}{R_0}} \quad (7)$$

between the partial irradiation resistance R_{part} and the full irradiation one R_{full}. Applying the formula to the recorded data

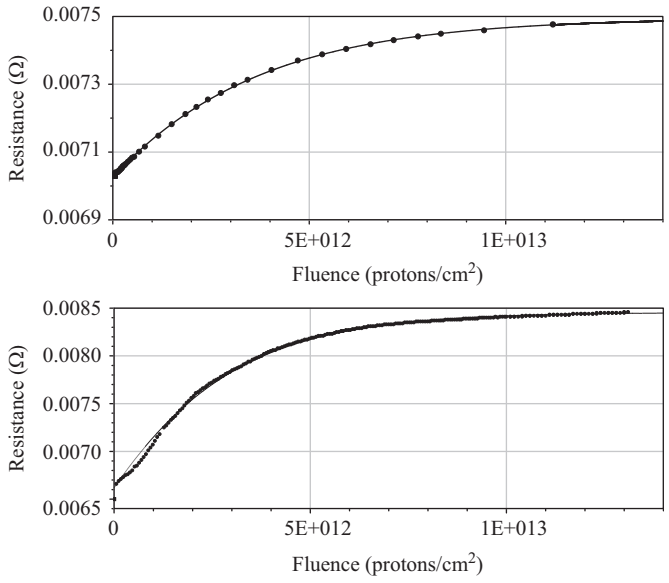

Fig. 19. Resistance of the partially irradiated MOS as a function of protons fluence: device irradiated with 5 MeV protons and exposed area 6.2% (upper); device irradiated with 5.5 MeV protons and exposed area 22.6% (lower).

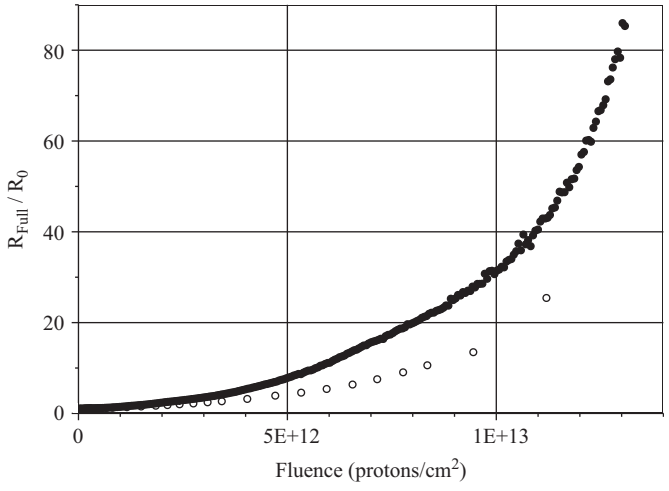

Fig. 20. Expected resistance variation of the MOS as a function of protons fluence extrapolating the partial irradiation results to the case of full irradiation: open circles correspond to the device irradiated with 5 MeV protons and the full circles correspond to the device irradiated with 5.5 MeV protons.

we find the plots in Fig. 20 which show that the resistance of the p-MOS would increase exponentially with the fluence, if fully irradiated. A similar behavior is reported in other measurements [15,16] although no attempt for a parametrization was done. The partially irradiated device resistance should then perform according to

$$R_{part}(F) = \frac{A \cdot R_0 e^{F/\varphi}}{A + (1-A) e^{F/\varphi}} \quad (8)$$

which is the form fitted to data in Fig. 19 with fitted constants $\varphi = 3.2 \times 10^{12}\ \mathrm{cm}^{-2}$ at 5.5 MeV and $\varphi = 2.9 \times 10^{12}\ \mathrm{cm}^{-2}$ at 5 MeV. Furthermore applying to Eq. (1) the assumption

$$\lim_{F \to \infty} R_{full}(F) = \infty \quad (9)$$

the maximum resistance obtainable in a partial irradiation is

$$R_{max} = \lim_{F \to \infty} R_{part}(F) = \frac{R_0}{1-A} \quad (10)$$

which reversed gives the fraction of irradiated area as a proof of validity

$$A = 1 - \frac{R_0}{R_{max}}. \quad (11)$$

The estimations of the irradiated areas obtained directly applying Eq. (11) to the data shown in Fig. 19 are 6.2% and 22.6% to be compared with the expected values of 7% and 25% from visual inspection of the device under the microscope.

5. Conclusions

The performance of a chamber used for proton irradiation of electronic devices was fully evaluated. The proton flux on the target is continuously monitored and recorded, either by direct measurement, if possible, or by an indirect determination based on a linear relationship among measurements on a series of collimators. In the latter case the error on the final fluence is only systematics and of the order of $\simeq 5\%$, mainly due to the quality of the beam line which shows important fluctuations during the irradiation.

The chamber was used to perform radiation resistance tests of a couple of electronic devices that could be deeply and completely tested. It is then ready to be used as a beam facility at the 7 MV Van de Graaf accelerator at the INFN laboratories in Legnaro.

Acknowledgments

The Proton Irradiation Chamber executive designs were produced by M. Zago of INFN Padova and all its mechanical pieces were actually built by A. Pitacco at the Mechanical Workshop of INFN Padova. We are really grateful to both of them, since the final object is a result of several approximations and could be obtained only modifying with their help the original concept several times.

References

[1] ZEUS Collaboration; M. Derrick, et al., Physics Letters B 293 (1992) 465.
[2] ZEUS Collaboration; U. Holm (Ed.), The ZEUS Detector. Status Report, unpublished, DESY, 1993; available on ⟨http://www-zeus.desy.de/bluebook/bluebook.html⟩.
[3] W. Hajdas, et al., Nuclear Instruments and Methods in Physics Research Section B 113 (1996) 54.
[4] J. Wyss, et al., Nuclear Instruments and Methods in Physics Research Section A 462 (2001) 426.
[5] G. Berger, et al., CYCLONE a Multipurpose Heavy Ion, Proton and Neutron SEE Test Site, 1997, RADECS Conference Data Workshop, p. 51.
[6] S. Agosteo, et al., Radiation Protection Dosimetry 126 (1–4) (2007) 210.

[7] S. Chatrchyan, et al., Journal of Instrumentation 3 (2008) S08004 (vol. 2, 1–334).
[8] P. Arce, et al., Nuclear Instruments and Methods in Physics Research Section A 534 (2004) 441.
[9] G. Lindström, et al., Nuclear Instruments and Methods in Physics Research Section A 426 (1999) 1.
[10] F. Hartmann, Evolution of Silicon Sensor Technology in Particle Physics, Springer, 2009.
[11] G. Lindström, et al., Silicon Detectors for Calorimetry-Developments for H1 at Hera, DESY Report 90–109, 1990.
[12] R. Wunstorf, et al., Nuclear Instruments and Methods in Physics Research Section A 377 (1996) 290.
[13] J. Wyss, et al., Nuclear Instruments and Methods in Physics Research Section A 497 (2001) 595.
[14] V. Barkhordarian, Power MOSFET Basics, International Rectifier Company.
[15] E. Bendada, Journal de Physique—III France 7 (1997) 2131.
[16] F. Faccio, IEEE Transactions on Nuclear Science 57 (4) (2010) 1790.